

Research Article

Open Access



Pore structure unveiling effect to boost lithium-selenium batteries: selenium confined in hierarchically porous carbon derived from aluminum based MOFs

Hong-Yan Li^{1,2,#}, Chao Li^{1,2,#}, Ying-Ying Wang^{1,2}, Wen-Da Dong³, Xi-Kun Zhang^{1,2}, Ming-Hui Sun^{1,2}, Yu Li^{3,*}, Bao-Lian Su^{1,2,3,*}

¹Laboratory of Inorganic Materials Chemistry (CMI), University of Namur, Namur B-5000, Belgium.

²Namur Institute of Structured Matter (NISM), University of Namur, Namur B-5000, Belgium.

³State Key Laboratory of Advanced Technology for Materials Synthesis and Processing, Wuhan University of Technology, Wuhan 430074, Hubei, China.

[#]These authors contributed equally.

***Correspondence to:** Prof. Bao-Lian Su, Laboratory of Inorganic Materials Chemistry (CMI), University of Namur, Rue de Bruxelles 61, Namur 5000, Belgium. E-mail: bao-lian.su@unamur.be/baoliansu@whut.edu.cn; Prof. Yu Li, State Key Laboratory of Advanced Technology for Materials Synthesis and Processing, Wuhan University of Technology, 122 Luoshi Road, Wuhan 430074, Hubei, China. E-mail: yu.li@whut.edu.cn

How to cite this article: Li HY, Li C, Wang YY, Dong WD, Zhang XK, Sun MH, Li Y, Su BL. Pore structure unveiling effect to boost lithium-selenium batteries: selenium confined in hierarchically porous carbon derived from aluminum based MOFs. *Chem Synth* 2023;3:30. <https://dx.doi.org/10.20517/cs.2023.16>

Received: 19 Mar 2023 **First Decision:** 07 Apr 2023 **Revised:** 10 May 2023 **Accepted:** 22 May 2023 **Published:** 9 Jun 2023

Academic Editors: Xiangdong Yao, Aicheng Chen **Copy Editor:** Dan Zhang **Production Editor:** Dan Zhang

Abstract

Lithium-selenium (Li-Se) batteries have attracted much attention in recent years because of their high volumetric capacity (3253 mA h cm⁻³) compared to the current commercial Li-ion battery. The shuttle effect and large volume variation during the electrochemical reactions limit its practical applications. The widely accepted strategy to reduce these drawbacks is confining selenium (Se) in porous carbon materials. However, how to boost electrochemical kinetics, reduce the shuttle effect and accommodate volume expansion for maximized battery performance still remains highly challenging. Herein, we synthesized three kinds of hierarchically porous carbon materials by facile pyrolysis of aluminum-based metal-organic frameworks (MOFs) with different porous networks. The large surface area and high pore volume can ensure the excellent polyselenides adsorption while tailoring the ratio between micropores and mesopores of the hierarchically porous hosts can highly enhance electrolyte and electron transportation, leading to excellent electrochemical performance with a capacity as high as 530.1 mA h g⁻¹ (Se@MIL-68-800) after 200 cycles, an excellent rate capability of 307 mA h g⁻¹ at 5 C, and a high



© The Author(s) 2023. **Open Access** This article is licensed under a Creative Commons Attribution 4.0 International License (<https://creativecommons.org/licenses/by/4.0/>), which permits unrestricted use, sharing, adaptation, distribution and reproduction in any medium or format, for any purpose, even commercially, as long as you give appropriate credit to the original author(s) and the source, provide a link to the Creative Commons license, and indicate if changes were made.



reversible capacity of 544 mA h g⁻¹ when current density returns to 0.1 C. The present invention not only provides a facile way to obtain hierarchically porous carbon materials from MOFs but also gives insights on tailoring micropores and mesopores proportion to maximize Li-Se battery performance for their practical industrial implementation.

Keywords: Metal-organic frameworks (MOFs), hierarchically porous carbon host, lithium-selenium (Li-Se) battery, physical adsorption

INTRODUCTION

Selenium (Se), from the same group as sulfur (S), has much higher electronic conductivity ($1 \times 10^{-3} \text{ S m}^{-1}$) compared with S ($5 \times 10^{-28} \text{ S m}^{-1}$) and comparable volumetric capacity (3253 mA h cm⁻³)^[1,2]. This makes Li-Se one of the most promising candidates and has attracted growing attention. However, the soluble intermediates lithium polyselenides (Li₂Se_n, $4 \leq n \leq 8$) in Li-Se battery still induce shuttle effects; in addition, the Se particles undergo volume expansion, and the final lithium selenide (Li₂Se) products are not conductive, leading to quick capacity decay, poor cycle performance, and low Coulombic efficiency (CE).

Confining Se in porous carbon materials is the most widely adopted and very efficient strategy to address these drawbacks. The porous carbon materials have significant influences on the final battery performances via highly improved conductivity of the electrode and increased reaction areas to adsorb the soluble polyselenides to relieve the shuttle effect and the volume expansion^[3-5]. The porous carbon materials with diverse morphologies and architectures, such as spheres^[6], 1D nanotubes^[7], 2D graphene^[8], 3D hierarchical structures^[9], hollow nanostructures^[10], and core-shell structures^[11], have been applied and shown improved performance of Li-Se batteries. According to the theoretical calculations using density functional theory (DFT), the size of the cyclo-Se₈ is determined to be 0.726 nm^[12]. The pores around this size are necessary for effectively accommodating and maintaining the loaded active Se in a well-infiltrated short chain-like amorphous state. Therefore, tailoring the pore size of porous carbon materials plays an important role in Li-Se batteries. Xin *et al.* reported microporous carbon coated on carbon nanotube (CNT) (CNT@MPC) composite consisting of numerous short-range-ordered slit pores of approximately 0.5 nm to confine Se in order to only form active small Se molecules^[13]. The electrochemical behavior of these confined Se chains revealed a reversible one-step reaction with lithium (Li) to yield highly active small Se molecules after the initial discharge. This significantly reduces the shuttle effect in the battery. Liu *et al.* prepared a microporous carbon polyhedral with a pore size of 1.1 nm to confine Se^[14]. The enlarged microporous carbon nanospheres with a pore size of around 1.3 nm were also utilized to confine Se^[6]. Excellent cycling stability has been observed because the micropores are beneficial for efficient polyselenides adsorption during the reaction. In a study on the effect of pore size on Li-S battery, Hippauf *et al.* experimentally demonstrated that the ultramicropores (less than 0.7 nm), supermicropores (between 0.7 and 2 nm), and mesopores behave quite differently to polysulfide adsorption in liquid phase with the help of UV/vis absorption spectroscopy^[15]. They reported that the ultramicroporous materials are up to eight times more efficient than mesoporous ones in adsorbing polysulfide. However, the solely microporous carbon is limited to the high proportion of Se loading, while it is detrimental to fast electrolyte diffusion. The typical ordered mesoporous carbon CMK-3 with a pore size of 3 nm and a high pore volume (1.276 cm³ g⁻¹) was proposed to confine Se^[16,17]. The mesoporous carbon can confine a higher amount of Se and promote quick electrolyte penetration. However, the cycling performance fades quickly because of polyselenides formation and easy dissolution in mesoporous carbons. Moreover, Liu *et al.* synthesized mesoporous carbon microspheres with different average pore sizes of 3.8, 5, 6.5, and 9.5 nm, using resorcinol-formaldehyde as a carbon precursor and silica sol as a hard template. The battery cycling performance decreases with increasing sizes of mesopores, and they proved that the size of mesoporous carbon host plays a key role in Se

immobilization^[18].

It is obvious that neither a microporous nor mesoporous structure alone could meet the requirements of a superior Li-Se battery with a high amount of Se and recycling stability performance at the same time. Other studies have focused on the bimodal or hierarchically porous carbons to combine the advantages of both micropores and mesopores, and such works have been reported^[19-21]. Park *et al.* introduced a self-sacrificed MOF template on polyacrylonitrile to obtain mesopores by direct carbonization and micropores by further chemical activation. They proved that the obtained porous carbon-containing simultaneously micropores and mesopores can achieve high cycling stability because the microporous part facilitates polyselenides trapping and high capacity, while the mesoporous part is beneficial for Se loading and electrolyte filtration^[19]. Our group also designed various hierarchically porous carbon, such as single ZIF-8 derived micro-meso-macropores carbon^[22], MWCNTs weaved MOF^[23], 3D hierarchically ordered porous carbon^[24], etc.^[25,26] All of them achieved good electrochemical performance. This demonstrates again that combining micropores and mesopores in a carbon host could be a good method to achieve high Se loading and enhance the adsorption of the polyselenides, leading to high cycle stability with a high energy density Li-Se battery. Proper pore size distribution of the host materials is critical to achieving good electrochemical performance of the battery. However, tailoring the ratio of the different size ranges of pores in porous carbon materials to get good cooperation needs to be deeply researched. It is thus highly valuable to investigate porous carbon materials with not only the best pores composition but also the optimized pore sizes ratio to maximize the synergy effects between different size pores.

MOFs have attracted increasing attention in the field of batteries because of their high surface area, uniform pore size, and chemical structure diversity^[27-30]. However, the low electrical conductivity of MOFs resulting in low capacity impedes their practical application. The pyrolysis of MOFs leads to much improved conductivity while keeping their defined porosity^[31-35]. The widely used MOFs for Li-Se batteries are based on zinc clusters, such as MOF-5 and ZIF-8. The zinc atoms can be conveniently removed during pyrolysis^[14,36]. However, the low boiling point of zinc tends to break the original order of micropores. Whereas for Co-MOF, Ni-MOF, and Fe-MOF, the formation of pores by the pyrolysis process will not be influenced by metal evaporation, and the remaining atoms of Co, Ni, and Fe have been proven to catalyze the discharge/charge reaction^[37-40]. In addition to the advantages same as Co-, Ni-, and Fe-MOF, aluminum-based MOFs are promising because they can form various MOFs with diverse morphologies with the same or different ligands in different synthesis conditions.

In this work, three kinds of hierarchically micro-mesoporous carbon materials have been successfully fabricated by facile aluminum-based MOF carbonization. The three aluminum-based MOFs originally are composed of the same metal cluster and similar ligands but with fully different pore configurations and volumes under different synthesis conditions. The obtained hierarchically micro-mesoporous carbon materials derived from these aluminum-based MOFs with large surface area and pore volume, interconnected pores, and the different proportions of micropores and mesopores. It is observed that the different ratios of micropores and mesopores can strongly impact the electrochemical properties of Li-Se batteries, leading to different charge-discharge capacities, rate capabilities, and recycling stability. By tailoring the ratio of micropores and mesopores, outstanding properties such as high loading of Se, high volume variation resistance during the electrochemical reaction, excellent fixing capacity of polyselenides, fast electrolyte, and electron transportation can be achieved, leading to a capacity as high as 530.1 mA h g⁻¹ after 200 cycles and excellent rate performance around 307 mA h g⁻¹ at 5 C. This work sheds light on a generic strategy to boost the electrochemical kinetics and to reduce the shuttle effect by tailoring the ratio of micropores and mesopores for Se confinement toward the practical implementation of Li-Se battery.

EXPERIMENTAL

Preparation of MIL-53 (Al)

MIL-53 (Al) was successfully synthesized through a hydrothermal reaction^[41]. In detail, aluminum nitrate nonahydrate [$\text{Al}(\text{NO}_3)_3 \cdot 9\text{H}_2\text{O}$, VWR, 3.9 g], terephthalic acid (TPA, VWR, 0.864 g), and deionized water (15.3 mL) were transferred into 50 mL Teflon-lined stainless steel autoclaves. The mixtures were then stirred for 30 mins and kept at 220 °C in an oven for three days for reaction. Afterward, the mixture was filtered, washed three times with deionized water and ethanol, and dried at 80 °C. The resulting white product was then purified in a muffle furnace (280 °C, three days). This high temperature can make sure complete removal of unreacted TPA species and the occluded TPA molecules within the structure. Finally, the light yellow powdery MIL-53(Al) was obtained.

Preparation of MIL-68 (Al)

The synthesis of MIL-68 (Al) was carried out following the reported work^[42,43]. Typically, TPA (VWR, 5 g) and aluminum chloride hexahydrate ($\text{AlCl}_3 \cdot 6\text{H}_2\text{O}$, VWR, 4.88 g) were dissolved in 300 mL of N, N-dimethylformamide (DMF, VWR). The mixture was then stirred for 2 h and transferred into autoclaves with Teflon insets, where it was kept at 130 °C for 18 h. Afterward, the mixture was cooled down to room temperature and collected by filtration. To remove any free acid that may still remain in the pores, the as-synthesized product was dispersed in 50 mL of DMF under stirring three times at room temperature. To further remove the DMF from the pores, the same procedure was repeated four times using 50 mL of methanol instead of DMF.

Preparation of MIL-100 (Al)

The synthesis of MIL-100 (Al) follows the reported protocol^[44,45]. In detail, 0.75 g $\text{Al}(\text{NO}_3)_3 \cdot 9\text{H}_2\text{O}$ and 0.37 g trimesic acid (H_3BTC , VWR) were mixed in a deionized water (10 mL) solution (pH = 1.9-2.0). More importantly, 0.192 g of DMF was added dropwise into this solution, and the quantity of DMF was 2.63 mmol based on their double CH_3 groups (pH = 1.9). After heating the mixture solution to 200 °C for about 4 h, a light yellow sample was obtained after filtration. Then, washing the powder three times with DMF and methanol, respectively, the purified MIL-100 (Al) was obtained after drying at 60 °C for 6-10 h.

Preparation of selenium@porous carbon composites

Each of the as-synthesized MIL-53 (Al), MIL-68 (Al), and MIL-100 (Al) was calcinated at 700, 800, and 900 °C, respectively, with a heating rate of 5 °C min⁻¹ for 4 h in an argon (Ar) atmosphere. To remove the aluminum species, the resulting black powder was immersed in a 4 M HCl aqueous solution at room temperature for 12 h. After washing with deionized water to remove any remaining acid, the products were dried in a vacuum oven overnight. The porous carbon materials derived from Al-MIL were labeled as MIL-53-700, MIL-53-800, MIL-53-900, MIL-68-700, MIL-68-800, MIL-68-900, and MIL-100-700, MIL-100-800, MIL-100-900, respectively. The Se-porous carbon composites were synthesized by a two-step melt-diffusion procedure. As all the samples calcined at 800 °C gave the highest surface area and highest pore volume, only the samples calcined at 800 °C were selected for the study on Se confinement. For example, with a weight ratio of 2:1, bulk Se (Sigma-Aldrich) and MIL-53-800 were thoroughly mixed by ball milling (labeled as Se-MIL-53-800). The mixture was then heated to 260 °C and maintained for 16 h, followed by heating to 300 °C for 4 h in a tube furnace filled with flowing Ar to obtain the composites. The final products were labeled as Se@MIL-53-800. The same procedures were carried out with MIL-68-800 and MIL-100-800, leading to the fabrication of Se@MIL-68-800 and Se@MIL-100-800, respectively.

Materials characterization

X-ray diffraction (XRD) patterns were obtained on a Panalytical with Cu K α radiation ($\lambda = 0.15406$ nm) with 45 kV and 30 mA. The scanning electron microscopy (SEM) observation was carried out using a JEOL

7500 F field-emission SEM. Transmission electron microscopy (TEM) images of the samples were recorded on microgrid copper mesh by using a TECNAI 10 at an acceleration voltage of 200 kV. Nitrogen (N_2) adsorption-desorption isotherms were obtained using an ASAP 2420 surface area & porosity analyzer at 77 K. The specific surface area was calculated by the Brunauer-Emmett-Teller (BET). The pore size distribution was calculated by the Barrett-Joyner-Halenda (BJH) method and the nonlocal density functional theory (NLDFT) analysis method. Thermogravimetric analysis (TGA) was carried out using a thermal analyzer (Setaram Labsys Evo) under a flow of N_2 with a temperature ramp of $5^\circ C\ min^{-1}$. X-ray photoelectron spectroscopy (XPS) characterization was carried out in a Thermo Fisher ESCALAB 250 Xi instrument with a monochromatic Al $K\alpha$ x-ray source (1486.6 eV). Raman spectra were collected by an Invia Repl (Renishaw, UK) under ambient conditions, from 2000 to $200\ cm^{-1}$ with 632.8 nm laser light.

Electrochemical measurements

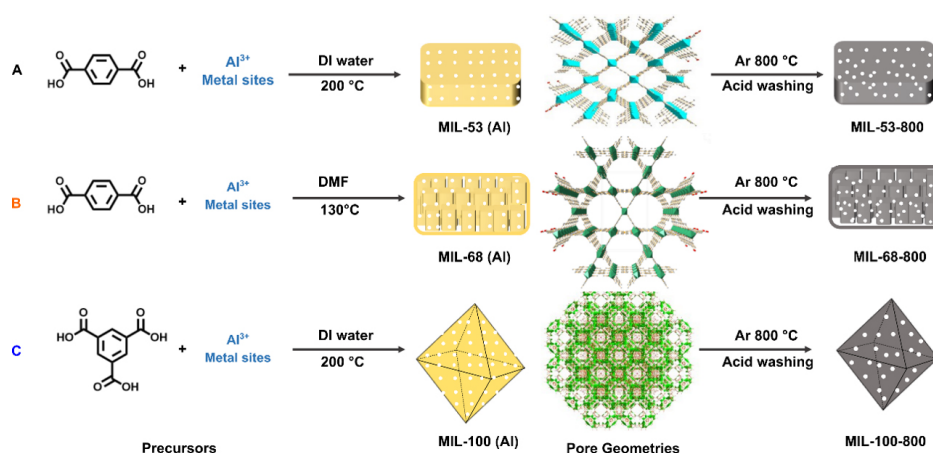
The electrochemical measurements were carried out at room temperature using CR2032 coin-type cells. The cathodes were prepared with a conventional slurry coating method^[40]. The slurry was prepared by mixing the active material, Super-P carbon (Timcal), and sodium alginate (SA, Sigma-Aldrich) at the weight ratio of 80:10:10 in deionized water. The reference pure Se cathode slurry was prepared by mixing commercial Se, Super-P carbon, and SA with a weight ratio of 60:30:10. The resulting slurry was coated onto an aluminum foil and dried in a vacuum at $60^\circ C$ one night. The coated aluminum foil was cut into discs with a diameter of 14 mm to obtain the Se cathode. The mass loading of Se on the cathode is approximately $1.5\ mg\ cm^{-2}$. The coin-type cells were assembled in an Ar-filled glovebox with moisture and oxygen concentrations lower than 1 ppm, using Li metal as the counter/reference electrode, glass fiber membrane as the separator, and 1 M Lithium bis(trifluoromethanesulfonyl)imide (LiTFSI, Solvay) in a mixture of dioxolane (DOL, Sigma-Aldrich) and dimethoxyethane (DME, Sigma-Aldrich) (1:1 in volume) with 1% $LiNO_3$ (Sigma-Aldrich) as the electrolyte. The galvanostatic discharge and charge experiments were performed on a battery tester (LAND) with a voltage window of 1.75-2.6 V vs. Li^+/Li at different current rates of 0.1, 0.2, 0.5, 1, 2, and 5 C (1 C = $75\ mA\ g^{-1}$). Cyclic voltammetry (CV) study (1.75-2.6 V vs. Li^+/Li , $0.1\ mV\ s^{-1}$) was performed using an electrochemical workstation Princeton VersaSTAT 3, beginning with discharge at 2.6 V. Electrochemical impedance spectroscopy (EIS) measurement was also conducted using Princeton VersaSTAT 3 with a frequency range between 100 kHz and 10 mHz with an AC voltage amplitude of 5 mV at open circuit voltage.

RESULTS AND DISCUSSION

Structural analysis

Scheme 1 illustrates the preparation process to (A) MIL-53 (Al), (B) MIL-68 (Al), and (C) MIL-100 (Al) and then to MIL-53-800, MIL-68-800, and MIL-100-800. MIL-53 (Al) (A) and MIL-68 (Al) (B) were synthesized with the same ligand (TPA) but with different solvents and temperatures, while MIL-100 (Al) (C) was synthesized with trimesic acid. These three MOFs exhibit fully different pore networks. In the case of MIL-53 (Al), only one 1D-rhombic type of pore with a size of 0.85 nm is found [**Scheme 1A**]^[46], while MIL-68 (Al) exhibits two different types of channels (triangular and hexagonal) with pore sizes of 0.5-0.85 nm and 1.6-1.7 nm, respectively [**Scheme 1B**]^[47]. As for MIL-100 (Al), its framework is formed by channels of micropores and mesopores of around 0.6 and 2.5-2.9 nm in diameter, respectively [**Scheme 1C**]^[48]. The MOF-derived porous carbon materials were obtained by the calcination of MOFs at high temperature in Ar, followed by an acid wash to remove aluminum.

The successful synthesis of aluminum-based MOFs, including MIL-53 (Al), MIL-68 (Al), and MIL-100 (Al), can be confirmed by the powder XRD patterns shown in **Supplementary Figure 1**. The representative peaks of MIL-53 (Al), MIL-68 (Al), and MIL-100 (Al) are the same as the simulated peaks, which are consistent with the previous reports^[41-44]. Following the pyrolysis, porous carbon materials are synthesized.



Scheme 1. Synthesis routes to (A) MIL-53 (Al); (B) MIL-68 (Al); and (C) MIL-100 (Al) with different precursors and thus to MIL-53-800, MIL-68-800, and MIL-100-800 by pyrolysis at 800 °C.

Supplementary Table 1 and **Supplementary Figure 2** summarize the surface area and pore volume information of samples before and after pyrolysis at 700, 800, and 900 °C. Notably, the surface area and pore volume of MIL-53 (Al) and MIL-68 (Al) decrease after pyrolysis at 700 °C due to the collapse of ordered micropores^[49]. However, the surface area and pore volume of MIL-100 (Al) increase owing to the stable trimesic acid ligand that could relieve the collapse of the MIL-100 (Al) structure. By increasing the pyrolysis temperature from 700 to 800 °C, the Al-MIL-derived porous carbon materials achieve higher surface area and pore volume for the reason of the gasification of carbon atoms. When the temperature rises to 900 °C, the surface area of MIL-53-900 and MIL-68-900 drops from 1566 to 413 and 1053 to 240 m² g⁻¹, and pore volume from 2.33 to 0.68 and 2.16 to 0.26 cm³ g⁻¹, respectively. The sharp decrease in the surface area and pore volume reflects the high collapse of the particle structure^[50-52]. The MIL-100-900 also shows a decrease in surface area and pore volume, but not as high as MIL-53-900 and MIL-68-900. That is because the trimesic acid ligands in the spatial configuration of MIL-100 (Al) help to resist high temperature to keep structural stability, which is commonly observed during the pyrolysis of ZIF series materials^[19,53]. To obtain enough pore space for Se loading and high surface area for electrochemical reactions, the samples from three Al-MOFs calcined at 800 °C showing the highest BET surface area and the pore volume were selected for Se confinement.

The morphologies of MOF-derived porous carbon materials are examined by SEM and TEM [Figure 1]. The morphology of MIL-53-800 remained intact after calcination compared with MIL-53 (Al) [Supplementary Figure 3A] and shows a massive porous structure with particle size ranging from several hundred nanometers to several micrometers [Figure 1A]. The TEM image [Figure 1B and its inset] presents the particle size and some empty space surrounded by carbon, which is consistent with the SEM result. Figure 1C confirmed the continuous amorphous carbon network with a microporous structure. The morphology of MIL-68-800 shows that the pyrolysis generates a highly porous structure [Figure 1D and E]. Compared with the original TEM morphology of MIL-68 (Al) in Supplementary Figure 3B, the big particle size of MIL-68-800 was composed of small carbon aggregates of 10-20 nm, where exists an interparticle mesopores structure. The micropores of MIL-68-800 can be observed in Figure 1F. MIL-100 (Al) showed a typical octahedron crystal structure with a size of 200-500 nm [Supplementary Figure 3C], and this morphology is still maintained after pyrolysis at 800 °C [Figure 1G]. Both mesopores and micropores were observed in Figure 1H and I. Consequently, the original morphologies can still be maintained after the pyrolysis of MOFs under appropriate conditions.

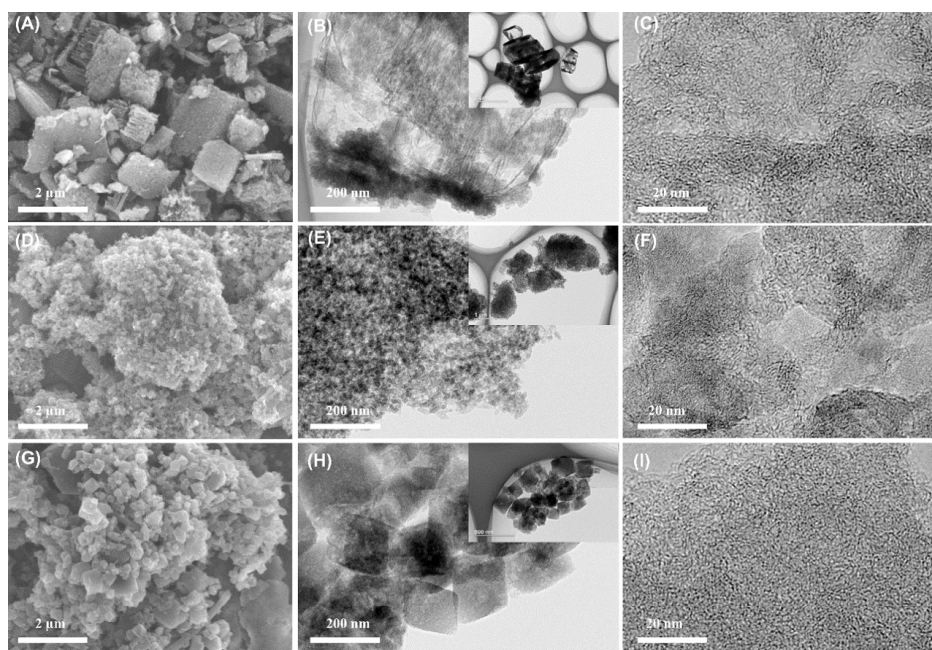


Figure 1. (A) SEM images and (B) (C) TEM images of MIL-53-800; (D) SEM images and (E) (F) TEM images of MIL-68-800; and (G) SEM images and (H) (I) TEM images of MIL-100-800.

The detailed pore size and cumulative pore volume distribution of these three selected MOF-derived porous carbon materials were measured by N_2 desorption-adsorption. The sharp increase of N_2 adsorption at low relative pressures ($p/p_0 < 0.01$) and hysteresis loop in the N_2 adsorption isotherms [Figure 2A] demonstrate that all three MOF-derived porous carbon materials contain micropores and mesopores^[54]. Compared with MIL-53-800 and MIL-68-800, MIL-100-800 has much more micropores but fewer mesopores. The cumulative pore size distribution of MIL-53-800, MIL-68-800, and MIL-100-800, calculated by the method of NLDFT, is shown in Figure 2B and converted into a histogram with four size zones in Figure 2C. All three samples show hierarchically porous structures with various pore sizes at different length scales. Four kinds of pores can be observed: ultramicropore (< 0.7 nm), supermicropore (0.7–2 nm), small mesopore (2–10 nm), and big mesopore (10–50 nm). Considering the ultramicropores (< 0.7 nm), the pore volume in this range of MIL-53-800 is $0.15 \text{ cm}^3 \text{ g}^{-1}$, which is similar to that of MIL-100-800 ($0.16 \text{ cm}^3 \text{ g}^{-1}$) while four times higher than that of MIL-68-800 ($0.04 \text{ cm}^3 \text{ g}^{-1}$). For the supermicropores (0.7–2 nm), the pore volume of MIL-53-800 ($0.15 \text{ cm}^3 \text{ g}^{-1}$) is comparable to that of MIL-68-800 ($0.12 \text{ cm}^3 \text{ g}^{-1}$) and half of that of MIL-100-800 ($0.33 \text{ cm}^3 \text{ g}^{-1}$). For the small mesopores (2–10 nm), the volume of MIL-53-800 is the biggest ($1.21 \text{ cm}^3 \text{ g}^{-1}$), which is two and six times higher than that of MIL-68-800 and MIL-100-800, respectively. The big mesoporous volume (10–50 nm) of MIL-53-800, MIL-68-800, and MIL-100-800 is 0.82, 1.41, and $0.14 \text{ cm}^3 \text{ g}^{-1}$, respectively. Due to the three-dimensional trimesic acid ligand, MIL-100-800 shows higher stability with more micropores, which represents 60% of the total volume. The harsh pyrolysis temperature and acid wash lead to the formation of high quantities of mesopores in MIL-53-800 and MIL-68-800. The detailed pore information of these three MIL-(53, 68, and 100)-800, including micropores and mesopores, is shown in Figure 2D–F. The pore size distribution and value of the pore volume are well consistent with the above-mentioned results.

For Se@MIL-(53, 68, 100)-800, the composites of Se and corresponding prepared porous carbon materials with a weight ratio of 2:1 were ball-milled and heated in Ar at 260°C . The Se was confined by the metal diffusion method, in which the commercial Se particles were melted to liquid that diffused from micropores

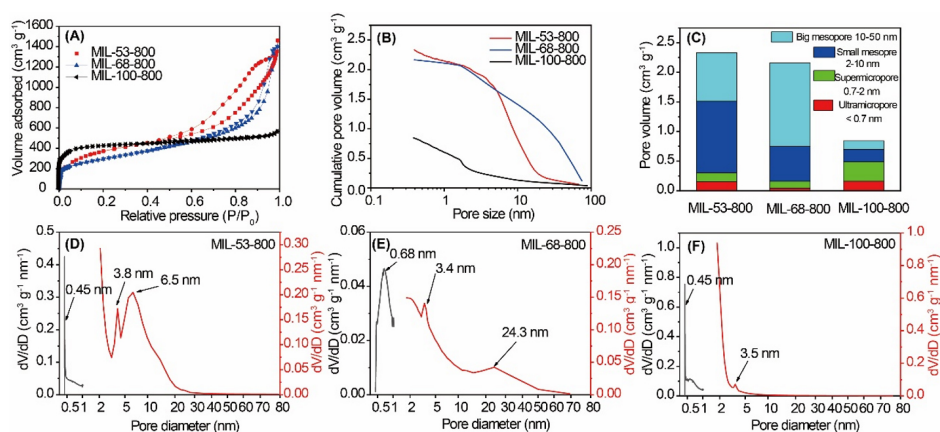


Figure 2. (A) N₂ adsorption-desorption isotherms at 77 K; (B) Cumulative pore size distribution and (C) Histogram of the size distribution of MIL-53-800, MIL-68-800, and MIL-100-800 based on nonlocal density functional theory (NLDFT) pore size analysis of nitrogen physisorption data; (D-F) Pore size distribution of MIL-53-800, MIL-68-800, and MIL-100-800, respectively.

to macropores with the help of the capillary effect. The successful confinement of Se and the exact weight ratio were studied by various characterization techniques. Figure 3A shows the XRD patterns of our MOF-derived samples after the confinement of Se. The pure Se exhibits its typical crystallized structure [PDF # 06-0362] with peaks at 23.5°, 29.7°, 41.3°, 43.6°, 45.4°, and 51.7°^[55]. The MIL-53-800 gives two big broad peaks, indicating the loss of the crystalline structure of MIL-53 (Al) after the pyrolysis process. The peaks from Se are clearly identified for Se-MIL-53-800 (the mixture of Se and MIL-53-800 by ball milling). It is the same for the mixtures of Se-MIL-68-800 and Se-MIL-100-800, as shown in Supplementary Figure 4. However, the peaks of Se are not observed with Se@MIL-53-800 after the melt-diffusion process, indicating the amorphous state of Se in the MIL-53-800 porous structure^[56,57]. The similar XRD patterns of Se@MIL-68-800 and Se@MIL-100-800 are observed, indicating that the Se remains in an amorphous state and effectively penetrated into the pores of MIL-68-800 and MIL-100-800, which will be confirmed by BET and EDX mapping measurements. However, there is a very weak peak of Se for Se@MIL-100-800, indicating the presence of a very small amount of crystalline Se in MIL-100-800. The probable reason would be the very limited pore volume of MIL-100-800 (0.84 cm³ g⁻¹) and a high proportion of micropores, as indicated in Figure 2C and Supplementary Table 1.

Raman spectra [Figure 3B] also proved the successful Se confinement within the obtained porous carbon materials, as indicated by the total disappearance peak of 236.8 cm⁻¹ for Se@MIL-53-800 and Se@MIL-68-800, which is the standard Raman peak of crystalline Se^[58]. A very small peak is still observed at 236.8 cm⁻¹ for Se@MIL-100-800, showing the presence of a very small amount of crystalline Se in this sample, which is perfectly consistent with XRD results. Furthermore, the peaks at approximately 1350 cm⁻¹ and 1584 cm⁻¹ are responsible for the carbon of MOF-derived porous carbon materials, which are also called D and G bands^[59]. The intensity of D and G bands is responsible for the disordered and graphite carbon^[60]. The similar intensity ratio (ID/IG) of around 1.02 for the three MOF-derived porous carbon materials indicates the similar ordered and disordered carbon state in these materials.

Supplementary Table 2 gives information on the surface area and pore volume before and after Se loading. The surface area sharply decreased from 1566 to 123 m² g⁻¹, 1053 to 139 m² g⁻¹, and 1412 to 21 m² g⁻¹ for MIL-53-800, MIL-68-800, and MIL-100-800, respectively, after Se infiltration. The sharp pore volume decreases from 2.33 to 0.33 cm³ g⁻¹, 2.16 to 0.6 cm³ g⁻¹, and 0.84 to 0.10 cm³ g⁻¹ for MIL-53-800, MIL-68-800, and MIL-100-800, respectively, were also observed. The drastic reduction of surface area and pore volume

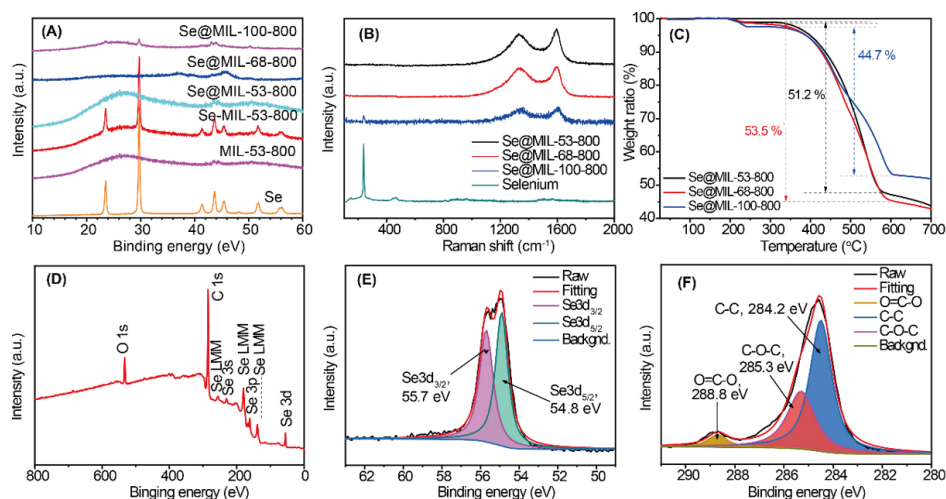


Figure 3. (A) XRD patterns of pure selenium, MIL-53-800, Se-MIL-53-800 mixture, Se@MIL-53-800, Se@MIL-68-800, and Se@MIL-100-800; (B) Raman spectrum of selenium, Se@MIL-53-800, Se@MIL-68-800, and Se@MIL-100-800; (C) TGA curves of Se@MIL-53-800, Se@MIL-68-800, and Se@MIL-100-800 under nitrogen with rate 5 °C min⁻¹. XPS spectrum of Se@MIL-53-800; (D) Survey scan curve (E) High-resolution Se3d and (F) C1s.

after Se infiltration directly evidences that the Se indeed diffuses into the pores of MOF-derived porous carbon materials. The SEM images after Se confinement and related energy dispersive X-ray spectroscopy EDX mapping are shown in [Supplementary Figure 5](#). The uniform dispersion of Se and carbon can obviously be proved by the overlapped images.

The content of Se confined in MOF-derived porous carbon materials was measured by TGA. As shown in [Figure 3C](#), the first weight loss is from 200 to 240 °C, responsible for the evaporation of bound water and moisture that adsorbed in micropores of MOF-derived porous carbon materials^[61]. The main weight losses start from 340 to 600 °C. The weight loss in this temperature zone corresponds to the dispersed Se in the pores^[62]. The Se@MIL-53-800 and Se@MIL-68-800 show the same shape with one important weight loss, while the MIL-100-800 at this range gives two weight losses with a turning point. That is due to the low pore volume and high micropores ratio of the MIL-100-800 composite; the diffusion of Se is limited by the lack of pathways, resulting in part of Se in the crystalline state. Compared with Se loaded in an amorphous state, the bulk Se confined with a crystalline state undergoes easier evaporation at lower temperature due to the weaker adsorption. While for MIL-53-800 and MIL-68-800, all the Se is in a well-dispersed amorphous state; thus, no turning point of the Se evaporation appears. This also indicates that micropores and mesopores are well interconnected, and tailoring the ratio between the micropores and mesopores of the hierarchically porous hosts has a significant influence on the system mass transfer. The total Se weight loss of Se@MIL-53-800, Se@MIL-68-800, and Se@MIL-100-800 are 53.5%, 51.2%, and 44.7%, respectively. As the pore volume of MIL-53-800 and MIL-68-800 is much higher than that of MIL-100-800, the higher loading of Se is observed in MIL-53-800 and MIL-68-800 than that in MIL-100-800.

The XPS is also applied to investigate the element composition, ratio, and electronic state of the specific elements. The survey scan of the Se@MIL-53-800 [[Figure 3D](#)] displays the peaks located at 533, 284, and 55.3 eV, corresponding to the O 1s, C 1s, and Se 3d, respectively. The high-resolution spectrum of Se 3d [[Figure 3E](#)] can be divided into two peaks (54.8 and 55.7 eV), corresponding to Se 3d_{5/2} and Se 3d_{3/2}, respectively^[63]. The peak of carbon [[Figure 3F](#)] can be deconvoluted into three peaks at 284.2, 285.3, and 288.8 eV, responsible for C-C, C-O, and C=O bonds, respectively^[64]. The similar survey scan and high-

resolution spectrum of carbon and Se of Se@MIL-68-800 and Se@MIL-100-800 are shown in [Supplementary Figure 6A](#) and [B](#) and [Supplementary Figure 6D-F](#), respectively. The weight ratio of Se from the survey scan of Se@MIL-53-800, Se@MIL-68-800, and Se@MIL-100-800 is 54.3%, 53.6%, and 45.4%, respectively, being in very excellent consistency with the results from TGA.

Electrochemical properties

The electrochemical properties of Se@MIL-53-800, Se@MIL-68-800, and Se@MIL-100-800 cathodes are presented in [Figure 4](#) and [Supplementary Figure 7](#), compared with pure Se electrode prepared as a reference. Cyclic voltammogram (CV) was collected at a scan rate of 0.1 mV s^{-1} with a potential range of 1.75–2.6 V vs. Li^+/Li in [Figure 4A](#) and [Supplementary Figure 7A-C](#). All the Se cathodes with MOF-derived porous carbon host show two obvious reduction peaks at approximately 2.1 and 1.95 V in the first cycle, relevant to the stepwise electrochemical reaction from Se to (Li_2Se_n) , finally to Li_2Se ^[65]. The oxidation peak, mainly at 2.25 V, and a shoulder peak at 2.35 V correspond to the Li_2Se back to Se with the intermediate Li_2Se_n , respectively. Compared with pure Se cathode, the reduction of Se@MIL-(53, 68, 100)-800 occurs on higher voltage in the first cycle, as the value labeled in [Figure 4A](#) and [Supplementary Figure 7A-C](#), reflecting the accelerated electrochemical reaction kinetics on these three cathodes. The reduction peak at 2.1 V shifts to a higher potential of 2.21 V after six cycles of battery operation [[Figure 4A](#)]. The shift of the first cathodic peak is due to the activation of Se particles and the formation of a stable solid electrolyte interphase (SEI) layer^[39,66,67]. The high potential shift of the first reduction peak means easier reduction reaction from Se to Li_2Se_n , indicating the Se cathodes were activated in the discharge/charge process. After activation through the first four cycles, the CV curves of these Se@MIL-X-800 (X = 53, 68, 100), overlapped well, demonstrating improved reversibility of these batteries^[68]. The compared result of these three MOF-derived cathodes on the 5th cycle is shown in [Figure 4B](#). It can be seen that Se@MIL-68-800 possesses the smallest oxidation/reduction potential gap (ΔV) and the highest current density than Se@MIL-53-800 and Se@MIL-100-800, suggesting the accelerated reaction kinetics in Se@MIL-68-800 cathode^[69]. It is worth noting that the pure Se cathode shows significantly different electrochemical behavior compared to the three MOF-derived porous carbon materials when used as carbon hosts for the Li-Se batteries. The pure Se cathode has the lowest reduction voltage at the first cycle due to the lack of pathways, while after five cycles, its reduction peak shifts to a higher voltage position than the other three cathodes. The phenomenon may be attributed to the easy diffusion and reaction of the polyselenides that have diffused out of the cathode, as they do not encounter significant interfacial barriers. Moreover, the detailed discharge/charge curves of the different electrodes at the 1st, 50th, 100th, 150th, and 200th cycles are also shown in [Figure 4C](#) and [Supplementary Figure 7D-F](#). The discharge curves show two typical platforms, in good consistence with the cyclic voltametric measurements containing two reduction peaks. The lowest gap between the discharge and charge platforms (overpotential) of Se@MIL-68-800 (0.1 V) among all the other three cathodes (Se@MIL-53 with 0.12 V, Se@MIL-100-800 with 0.17 V, and pure Se with 0.17 V) means its lowest polarization compared to the other three batteries, indicating the smallest reaction energy barrier^[70].

The cycling performance and CE were evaluated at 0.2 C between 1.75–2.6 V. The initial discharge capacity of Se@MIL-53-800, Se@MIL-68-800, and Se@MIL-100-800 shows much higher values of 704.5, 648.3, and 473.7 mA h g^{-1} , respectively, compared to 342.3 mA h g^{-1} of pure Se cathode. The much higher initial capacity than pure Se cathode indicates the much higher utilization efficiency of Se for Se@MIL-53-800, Se@MIL-68-800, and Se@MIL-100-800. Because the highly porous carbon can lead to a large dispersion of Se in the carbon host system, facilitating the contact between carbon and Se for better electrochemical activity. The initial discharge capacity of Se@MIL-53-800 is higher than the theoretical value (675 mA h g^{-1}), and that of Se@MIL-68-800 is very similar to their theoretical value, while the Se@MIL-100-800 achieves a capacity value that is far from its theoretical value. This is due to the lack of interconnected micro-mesopores constructed electrolyte pathways for the Se@MIL-100-800 cathode, in spite of its high CE value

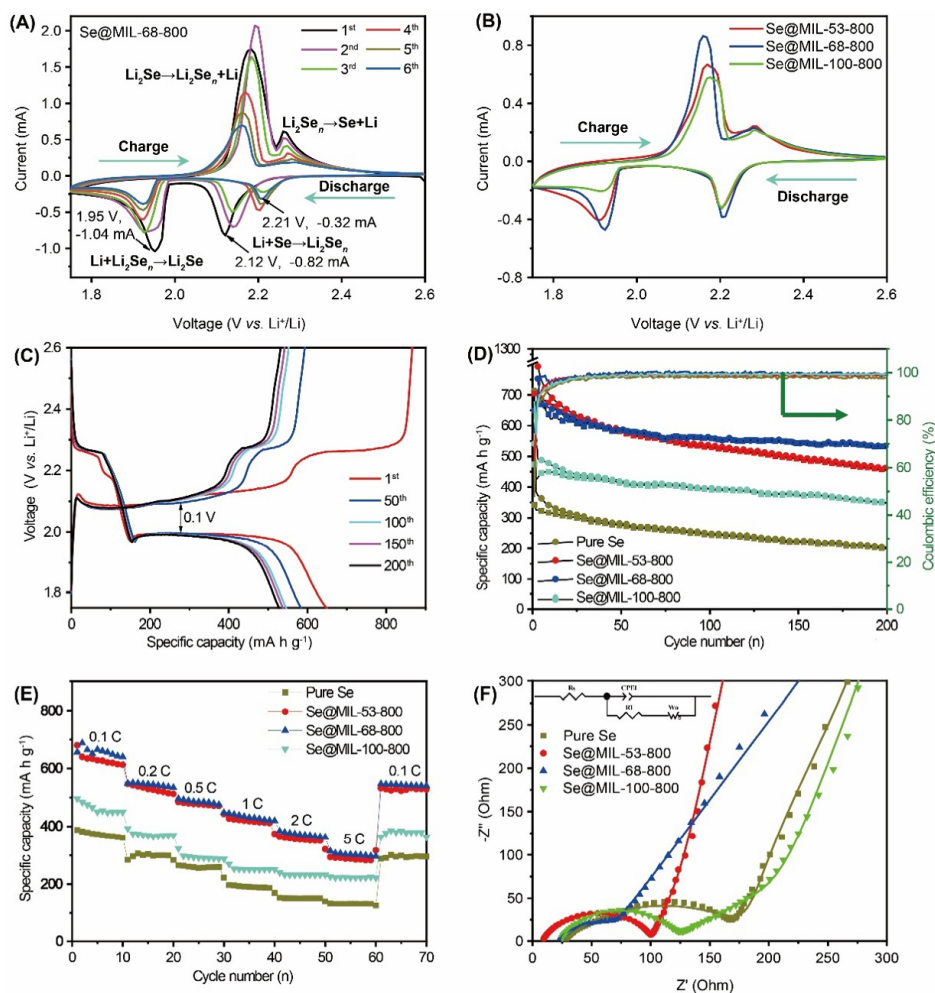


Figure 4. Cyclic voltammetry curves of (A) Se@MIL-53-800 and (B) Compared CV result of different cathodes in the 5th cycle at a voltage of 1.75–2.6 V vs. Li⁺/Li with the scan rate of 0.1 mV s⁻¹; (C) The discharge/charge curves at the voltage of 1.75–2.6 V vs. Li⁺/Li with the current density of 0.2 C. The electrochemical properties of pure Se, Se@MIL-53-800, Se@MIL-68-800, and Se@MIL-100-800 cathodes in Li-Se cell; (D) Cycling performance and corresponding Coulombic efficiency at 0.2 C; (E) Rate capability and (F) Nyquist plots of these four different cathodes at fresh state.

of 87.5%. The initial CEs of Se@MIL-53-800 and Se@MIL-68-800 are 62.9% and 74.8%, respectively. The high initial capacity and low CE of these two cathodes can be attributed to the irreversible formation process of the SEI layer and electrolyte decomposition on the matrix materials in the first cycle^[71]. The CE of Se@MIL-68-800 quickly increases to more than 95% in the first three cycles, which is attributed to the rapid formation of a stable SEI layer, leading to the decrease of irreversible side reaction between the Se cathode and electrolyte. This is much faster than that of Se@MIL-53-800, Se@MIL-100-800, and pure Se cathode to be stabilized because of its good Se dispersion and strong adsorption to polyselenides by optimized pores distribution^[72]. As shown in Figure 4D, the discharge capacity of Se@MIL-53-800, Se@MIL-68-800, Se@MIL-100-800, and pure Se cathodes after 200 cycles is 457, 530.1, 347.9, and 199.3 mA h g⁻¹, respectively. The Se@MIL-53-800 shows comparable capacity in the first several cycles as Se@MIL-68-800. However, Se@MIL-68-800 keeps the capacity much better with high cycling stability after 200 cycles.

The rate capabilities of these three MOF-derived cathodes and the reference pure Se cathode is shown in Figure 4E. The capacity decreases with increased current density due to the polarization and the limited

utilization of Se^[73]. The Se@MIL-68-800 and Se@MIL-53-800 exhibit very similar high discharge capacities, with the current density increasing from 0.1 C to 5 C due to the high proportion of mesopores and macropores in the corresponding two host materials. The capacity value of Se@MIL-68-800 (307 mA h g⁻¹) is higher than that of Se@MIL-53-800 (292 mA h g⁻¹) at the current density of 5 C, reflecting its better pore size cooperation to accelerate the transportation of electrons/ions. When the current density returns to 0.1 C, a high reversible capacity of 544 mA h g⁻¹ is achieved for Se@MIL-68-800, indicating fast electrode reaction kinetics. The best rate capability of Se@MIL-68-800 is probably stemmed from its large proportion of large mesopores, which can ensure the rapid electrolyte transportation and shorten the distance between active Se in the cathode. The capacity of Se@MIL-100-800 and pure Se cathode can be only 220 and 130 mA h g⁻¹ at 5 C and the reversible capacities of 380 and 295 mA h g⁻¹ at 0.1 C, respectively, demonstrating deteriorated rate performance because of inappropriate porous structures. From the cycling performance, CE, and rate capability test, it is clearly seen that Se@MIL-68-800 performs better than Se@MIL-53-800, Se@MIL-100-800, and pure Se in Li-Se battery. Moreover, compared with the reported papers with similar Se host materials^[74-76], the Se@MIL-68-800 cathode achieves a promising electrochemical performance, as shown in [Supplementary Table 3](#).

To obtain further insight into the mechanism of improved cycle and rate performance, EIS analysis was carried out [[Figure 4F](#)]. The curves are composed of a semicircle at high frequency followed by a straight line at low frequency. The start point corresponds to the Ohmic resistance (R_{Ω}) of the whole battery^[77-79], while the diameter of the semicircle corresponds to the interface resistance between electrode and electrolyte (also called charge transfer resistance, R_{ct})^[80-82]. The fitted circuit diagram is shown in the inset. The interface resistance has a huge influence on the Li-ion and electron transportation. The R_{ct} values of Se@MIL-53-800, Se@MIL-68-800, Se@MIL-100-800, and pure Se cathode were 95, 48, 93, and 162 Ω , respectively. The smallest of Se@MIL-68-800 indicates its fastest reaction kinetics in the discharge/charge process.

[Figure 5](#) schematically illustrates the mechanism of the MIL-53-800, MIL-68-800, and MIL-100-800 as hosts for Se. For the Se@MIL-53-800 composites (I), there are some interconnected large mesopores that traverse the whole particles, along with a large number of small mesopores and numerous micropores [[Figure 2C](#)] to carry selenium. This designed structure could ensure a high rate of electrolyte transfer and enough space for Se loading and reaction sites. For Se@MIL-68-800 (II), the difference in pores distribution compared to Se@MIL-53-800 is that the large mesopores occupy a larger proportion, while small mesopores are less abundant. At the same time, the number of micropores becomes a little bit less [[Figure 2C](#)], but it is still enough for Se loading. The enlarged pathways accelerate the mass transfer of ions and electrolytes. In the case of Se@MIL-100-800 (III), although there are plentiful micropores for loading Se, the lack of pathway of mesopores leads to slow mass transfer and inadequate reaction. The compromise between the efficient adsorption of polyselenides, fast electrolyte transfer, and fast Li-ion transportation should be well considered. Therefore, the balance of micropores (providing space for Se loading, reaction sites, and strong adsorption to polyselenides) and mesopores (pathways for Se loading and ions/electrons transportation) is critical for high reaction kinetics achievement. Se@MIL-68-800 cathode achieved the best electrochemical performances due to the optimized distribution and ratio of micropores and mesopores. The excellent electrochemical performances of Se@MIL-68-800 can be attributed to the following reasons: (1) High specific surface area and pore volume of high conductivity carbon materials are necessary to achieve good performance due to better Se dispersion, high utilization, and volume expansion suppression; (2) The rational range of micropores that provide Se loading space and interconnected with micropores-mesopores that shorten the pathways of the electrolyte can maximize the battery performance; (3) Most importantly, the favorable MOF-derived hierarchically porous carbon including the optimized ratio of micropores and

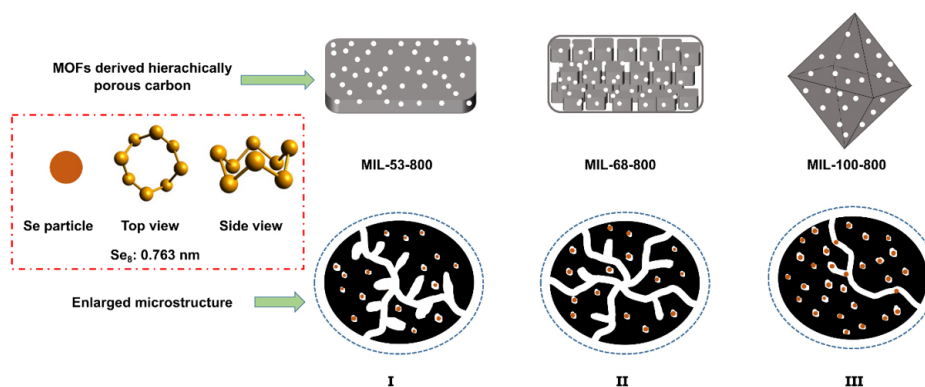


Figure 5. Schematic mechanism of the MOF-derived hierarchically porous carbon for selenium confinement and the synergistic effect of micropores and mesopores during the electrochemical reaction.

mesopores can achieve more efficient suppression of polyselenides dissolution and fast electrolyte transportation at the same time.

CONCLUSIONS

Hierarchically micro-mesoporous carbon materials have been synthesized to confine Se by facile carbonization of three kinds of aluminum-based MOFs. The hierarchically micro-mesoporous carbon structure can confine Se well and alleviate the volume expansion, especially enhancing the adsorption of soluble polyselenides, leading to improved battery performance. Especially, the micropores can efficiently decrease the polyselenides dissolution to inhibit the shuttle effect, and the mesopores interconnected with micropores can lead to good electrolyte transportation. These synergistic hierarchically micro-mesoporous characteristics with a well-balanced ratio of micropores and mesopores achieved a capacity of $456.6 \text{ mA h g}^{-1}$ for Se@MIL-53-800 and $530.1 \text{ mA h g}^{-1}$ for Se@MIL-68-800, compared to $348.4 \text{ mA h g}^{-1}$ for their fewer mesopore counterparts Se@MIL-100-800 and $199.3 \text{ mA h g}^{-1}$ for pure Se cathode after 200 cycles. The Se@MIL-68-800 also showed very good rate performance around 307 mA h g^{-1} at 5 C and a high reversible capacity of 544 mA h g^{-1} when back to 0.1 C. Furthermore, the electrochemical performance of the battery should be further improved through the modification of electrolytes to better match the prepared Se cathode^[83-85]. Our strategy not only provides a facile way to obtain hierarchically porous carbon from MOFs but also gives insights on how to regulate the proportion of micropores and mesopores to achieve a better Li-Se or Li-S battery performance.

DECLARATIONS

Acknowledgments

Hongyan Li and Chao Li thank the financial support from the China Scholarship Council (CSC) and a scholarship from the Laboratory of Inorganic Materials Chemistry, Université de Namur. The authors thank the help of battery impedance analysis from Prof. Alexandru Vlad (Institute of Condensed Matter and Nanosciences, Université catholique de Louvain) and the support of bis(trifluoromethane)sulfonimide Li salt from Solvey company. The authors thank the help of TEM characterization from Mr. Weichun Huang (Shenzhen Engineering Laboratory of Phosphorene and Optoelectronics, Shenzhen University).

Authors' contributions

Provided financial support: Su BL, Li Y

Revised and finalized the manuscript: Su BL, Li Y

Designed the samples, performed experiments, and wrote the paper with support from: Su BL, Li Y, Li HY, Li C

Gave the experimental guidance and advice: Sun MH, Dong WD

Provided 3D image rendering: Wang YY

Help for data supplement: Zhang XK, Dong WD

All authors contributed to the general discussion.

Availability of data and materials

The detailed materials and methods in the experiment were listed in the Supplementary Materials. Other raw data that support the findings of this study are available from the corresponding author upon reasonable request.

Financial support and sponsorship

This work is supported by the National Key R&D Program of China (2016YFA0202602, 2021YFE0115800), National Key R&D Program, Intergovernmental Technological Innovation Special Cooperation Project: WBI International (Wallonia-Brussels)-Most (2021YFE0115800 and SUB/2021/IND493971/524448), National Natural Science Foundation of China (U20A20122, 52103285), Program of Introducing Talents of Discipline to Universities-Plan 111 from the Ministry of Science and Technology and the Ministry of Education of China (Grant No. B20002).

Conflicts of interest

All authors declared that there are no conflicts of interest.

Ethical approval and consent to participate

Not applicable.

Consent for publication

Not applicable.

Copyright

© The Author(s) 2023.

REFERENCES

1. Yang CP, Yin YX, Guo YG. Elemental selenium for electrochemical energy storage. *J Phys Chem Lett* 2015;6:256-66. [DOI](#) [PubMed](#)
2. Abouimrane A, Dambournet D, Chapman KW, Chupas PJ, Weng W, Amine K. A new class of lithium and sodium rechargeable batteries based on selenium and selenium-sulfur as a positive electrode. *J Am Chem Soc* 2012;134:4505-8. [DOI](#) [PubMed](#)
3. Manthiram A, Fu Y, Su YS. Challenges and prospects of lithium-sulfur batteries. *Acc Chem Res* 2013;46:1125-34. [DOI](#) [PubMed](#)
4. Wang D, Zeng Q, Zhou G, et al. Carbon-sulfur composites for Li-S batteries: status and prospects. *J Mater Chem A* 2013;1:9382. [DOI](#)
5. Paraknowitsch JP, Thomas A. Doping carbons beyond nitrogen: an overview of advanced heteroatom doped carbons with boron, sulphur and phosphorus for energy applications. *Energy Environ Sci* 2013;6:2839. [DOI](#)
6. Li Z, Yuan L, Yi Z, Liu Y, Huang Y. Confined selenium within porous carbon nanospheres as cathode for advanced Li-Se batteries. *Nano Energy* 2014;9:229-36. [DOI](#)
7. Wang H, Li S, Chen Z, Liu HK, Guo Z. A novel type of one-dimensional organic selenium-containing fiber with superior performance for lithium-selenium and sodium-selenium batteries. *RSC Adv* 2014;4:61673-8. [DOI](#)
8. Youn HC, Jeong JH, Roh KC, Kim KB. Graphene-selenium hybrid microballs as cathode materials for high-performance lithium-selenium secondary battery applications. *Sci Rep* 2016;6:30865. [DOI](#) [PubMed](#) [PMC](#)
9. He J, Chen Y, Lv W, et al. Three-dimensional hierarchical graphene-CNT@Se: a highly efficient freestanding cathode for Li-Se batteries. *ACS Energy Lett* 2016;1:16-20. [DOI](#)
10. Fan S, Zhang Y, Li S, Lan T, Xu J. Hollow selenium encapsulated into 3D graphene hydrogels for lithium-selenium batteries with high rate performance and cycling stability. *RSC Adv* 2017;7:21281-6. [DOI](#)
11. Fan JM, Chen JJ, Zhang Q, et al. An amorphous carbon nitride composite derived from ZIF-8 as anode material for sodium-ion batteries. *Chem Sus Chem* 2015;8:1856-61. [DOI](#)
12. Wang H, Jiang Y, Manthiram A. Long cycle life, low self-discharge sodium-selenium batteries with high selenium loading and

- suppressed polyselenide shuttling. *Adv Energy Mater* 2018;8:1701953. DOI
13. Xin S, Yu L, You Y, et al. The Electrochemistry with Lithium versus sodium of selenium confined to slit micropores in carbon. *Nano Lett* 2016;16:4560-8. DOI
 14. Liu Y, Si L, Zhou X, et al. A selenium-confined microporous carbon cathode for ultrastable lithium-selenium batteries. *J Mater Chem A* 2014;2:17735-9. DOI
 15. Hippauf F, Nickel W, Hao G, et al. The importance of pore size and surface polarity for polysulfide adsorption in lithium sulfur batteries. *Adv Mater Interfaces* 2016;3:1600508. DOI
 16. Yang CP, Xin S, Yin YX, Ye H, Zhang J, Guo YG. An advanced selenium-carbon cathode for rechargeable lithium-selenium batteries. *Angew Chem Int Ed Engl* 2013;52:8363-7. DOI
 17. Ji X, Lee KT, Nazar LF. A highly ordered nanostructured carbon-sulphur cathode for lithium-sulphur batteries. *Nat Mater* 2009;8:500-6. DOI PubMed
 18. Liu L, Wei Y, Zhang C, et al. Enhanced electrochemical performances of mesoporous carbon microsphere/selenium composites by controlling the pore structure and nitrogen doping. *Electrochimica Acta* 2015;153:140-8. DOI
 19. Park S, Park J, Kang YC. Selenium-infiltrated metal-organic framework-derived porous carbon nanofibers comprising interconnected bimodal pores for Li-Se batteries with high capacity and rate performance. *J Mater Chem A* 2018;6:1028-36. DOI
 20. Liu T, Dai C, Jia M, et al. Selenium embedded in metal-organic framework derived hollow hierarchical porous carbon spheres for advanced lithium-selenium batteries. *ACS Appl Mater Interfaces* 2016;8:16063-70. DOI
 21. Xia W, Qiu B, Xia D, Zou R. Facile preparation of hierarchically porous carbons from metal-organic gels and their application in energy storage. *Sci Rep* 2013;3:1935. DOI PubMed PMC
 22. Li H, Dong W, Li C, et al. Boosting reaction kinetics and shuttle effect suppression by single crystal MOF-derived N-doped ordered hierarchically porous carbon for high performance Li-Se battery. *Sci China Mater* 2022;65:2975-88. DOI
 23. Li C, Wang Y, Li H, et al. Weaving 3D highly conductive hierarchically interconnected nanoporous web by threading MOF crystals onto multi walled carbon nanotubes for high performance Li-Se battery. *J Energy Chem* 2021;59:396-404. DOI
 24. Li H, Dong W, Li C, et al. Three-dimensional ordered hierarchically porous carbon materials for high performance Li-Se battery. *J Energy Chem* 2022;68:624-36. DOI
 25. Song JP, Wu L, Dong WD, et al. MOF-derived nitrogen-doped core-shell hierarchical porous carbon confining selenium for advanced lithium-selenium batteries. *Nanoscale* 2019;11:6970-81. DOI
 26. Dong WD, Yu WB, Xia FJ, et al. Melamine-based polymer networks enabled N, O, S Co-doped defect-rich hierarchically porous carbon nanobelts for stable and long-cycle Li-ion and Li-Se batteries. *J Colloid Interface Sci* 2021;582:60-9. DOI
 27. Zhao Y, Song Z, Li X, et al. Metal organic frameworks for energy storage and conversion. *Energy Storage Mater* 2016;2:35-62. DOI
 28. Wang L, Han Y, Feng X, Zhou J, Qi P, Wang B. Metal-organic frameworks for energy storage: Batteries and supercapacitors. *Coord Chem Rev* 2016;307:361-81. DOI
 29. Liu X, Sun T, Hu J, Wang S. Composites of metal-organic frameworks and carbon-based materials: preparations, functionalities and applications. *J Mater Chem A* 2016;4:3584-616. DOI
 30. Xu J, Lawson T, Fan H, Su D, Wang G. Updated metal compounds (MOFs, -S, -OH, -N, -C) used as cathode materials for lithium-sulfur batteries. *Adv Energy Mater* 2018;8:1702607. DOI
 31. Tang J, Yamauchi Y. Carbon materials: MOF morphologies in control. *Nat Chem* 2016;8:638-9. DOI PubMed
 32. Dang S, Zhu Q, Xu Q. Nanomaterials derived from metal-organic frameworks. *Nat Rev Mater* 2018;3. DOI
 33. Lim S, Suh K, Kim Y, et al. Porous carbon materials with a controllable surface area synthesized from metal-organic frameworks. *Chem Commun* 2012;48:7447-9. DOI
 34. Chaikittisilp W, Ariga K, Yamauchi Y. A new family of carbon materials: synthesis of MOF-derived nanoporous carbons and their promising applications. *J Mater Chem A* 2013;1:14-9. DOI
 35. Wu HB, Lou XWD. Metal-organic frameworks and their derived materials for electrochemical energy storage and conversion: promises and challenges. *Sci Adv* 2017;3:eaap9252. DOI
 36. Lai Y, Gan Y, Zhang Z, Chen W, Li J. Metal-organic frameworks-derived mesoporous carbon for high performance lithium-selenium battery. *Electrochimica Acta* 2014;146:134-41. DOI
 37. Guo L, Sun J, Sun X, Zhang J, Hou L, Yuan C. Construction of 1D conductive Ni-MOF nanorods with fast Li⁺ kinetic diffusion and stable high-rate capacities as an anode for lithium ion batteries. *Nanoscale Adv* 2019;1:4688-91. DOI PubMed PMC
 38. Cai S, Meng Z, Cheng Y, et al. Three dimension Ni/Co-decorated N-doped hierarchically porous carbon derived from metal-organic frameworks as trifunctional catalysts for Zn-air battery and microbial fuel cells. *Electrochimica Acta* 2021;395:139074. DOI
 39. Xu Q, Liu T, Li Y, et al. Selenium encapsulated into metal-organic frameworks derived N-doped porous carbon polyhedrons as cathode for Na-Se batteries. *ACS Appl Mater Interfaces* 2017;9:41339-46. DOI
 40. He J, Lv W, Chen Y, et al. Three-dimensional hierarchical C-Co-N/Se derived from metal-organic framework as superior cathode for Li-Se batteries. *J Power Sources* 2017;363:103-9. DOI
 41. Loiseau T, Serre C, Huguenard C, et al. A rationale for the large breathing of the porous aluminum terephthalate (MIL-53) upon hydration. *Chemistry* 2004;10:1373-82. DOI
 42. Volkringer C, Meddouri M, Loiseau T, et al. The Kagomé topology of the gallium and indium metal-organic framework types with a MIL-68 structure: synthesis, XRD, solid-state NMR characterizations, and hydrogen adsorption. *Inorg Chem* 2008;47:11892-901. DOI

43. Yang Q, Vaesen S, Vishnuvarthan M, et al. Probing the adsorption performance of the hybrid porous MIL-68(Al): a synergic combination of experimental and modelling tools. *J Mater Chem* 2012;22:10210. DOI
44. Wang J, Yang J, Krishna R, Yang T, Deng S. A versatile synthesis of metal-organic framework-derived porous carbons for CO₂ capture and gas separation. *J Mater Chem A* 2016;4:19095-106. DOI
45. Yang J, Wang J, Deng S, Li J. Improved synthesis of trigone trimer cluster metal organic framework MIL-100Al by a later entry of methyl groups. *Chem Commun* 2016;52:725-8. DOI PubMed
46. Seoane B, Téllez C, Coronas J, Staudt C. NH₂-MIL-53(Al) and NH₂-MIL-101(Al) in sulfur-containing copolyimide mixed matrix membranes for gas separation. *Sep Purif Technol* 2013;111:72-81. DOI
47. Perea-cachero A, Romero E, Téllez C, Coronas J. Retracted article: insight into the reversible structural crystalline-state transformation from MIL-53(Al) to MIL-68(Al). *Cryst Eng Comm* 2018;20:402-6. DOI
48. García Márquez A, Demessence A, Platero-prats AE, et al. Green microwave synthesis of MIL-100(Al, Cr, Fe) nanoparticles for thin-film elaboration. *Eur J Inorg Chem* 2012;2012:5165-74. DOI
49. Zhou H, Zheng M, Tang H, Xu B, Tang Y, Pang H. Amorphous intermediate derivative from ZIF-67 and its outstanding electrocatalytic activity. *Small* 2020;16:e1904252. DOI PubMed
50. Zhang X, Li H, Lv X, et al. Facile Synthesis of highly efficient amorphous Mn-MIL-100 catalysts: formation mechanism and structure changes during application in CO oxidation. *Chemistry* 2018;24:8822-32. DOI
51. Zhou QY, Zhang Z, Cai JJ, et al. Template-guided synthesis of Co nanoparticles embedded in hollow nitrogen doped carbon tubes as a highly efficient catalyst for rechargeable Zn-air batteries. *Nano Energy* 2020;71:104592. DOI
52. Chen B, He X, Yin F, et al. MO-Co@N-Doped Carbon (M=Zn or Co): vital roles of inactive zn and highly efficient activity toward oxygen reduction/evolution reactions for rechargeable Zn-Air battery. *Adv Funct Mater* 2017;27:1700795. DOI
53. Jiang Y, Liu H, Tan X, et al. Monoclinic ZIF-8 nanosheet-derived 2D carbon nanosheets as sulfur immobilizer for high-performance lithium sulfur batteries. *ACS Appl Mater Interfaces* 2017;9:25239-49. DOI
54. Bardestani R, Patience GS, Kaliaguine S. Experimental methods in chemical engineering: specific surface area and pore size distribution measurements-BET, BJH, and DFT. *Can J Chem Eng* 2019;97:2781-91. DOI
55. Li Z, Yin L. MOF-derived, N-doped, hierarchically porous carbon sponges as immobilizers to confine selenium as cathodes for Li-Se batteries with superior storage capacity and perfect cycling stability. *Nanoscale* 2015;7:9597-606. DOI
56. Qu Y, Zhang Z, Jiang S, et al. Confining selenium in nitrogen-containing hierarchical porous carbon for high-rate rechargeable lithium-selenium batteries. *J Mater Chem A* 2014;2:12255. DOI
57. Xia Z, Zhang J, Fan M, Lv C, Chen Z, Li C. Se with Se-C bonds encapsulated in a honeycomb 3D porous carbon as an excellent performance cathode for Li-Se batteries. *New Carbon Materials* 2023;38:190-8. DOI
58. Zhou X, Gao P, Sun S, et al. Amorphous, crystalline and crystalline/amorphous selenium nanowires and their different (De)lithiation mechanisms. *Chem Mater* 2015;27:6730-6. DOI
59. Ribeiro-soares J, Oliveros M, Garin C, et al. Structural analysis of polycrystalline graphene systems by Raman spectroscopy. *Carbon* 2015;95:646-52. DOI
60. Liu Y, Lu YX, Xu YS, et al. Pitch-derived soft carbon as stable anode material for potassium ion batteries. *Adv Mater* 2020;32:e2000505. DOI
61. Zhou J, Yang J, Xu Z, Zhang T, Chen Z, Wang J. A high performance lithium-selenium battery using a microporous carbon confined selenium cathode and a compatible electrolyte. *J Mater Chem A* 2017;5:9350-7. DOI
62. Wang X, Zhang Z, Qu Y, Wang G, Lai Y, Li J. Solution-based synthesis of multi-walled carbon nanotube/selenium composites for high performance lithium-selenium battery. *J Power Sources* 2015;287:247-52. DOI
63. Wang P, Sun F, Xiong S, et al. WSe₂ Flakelets on N-doped graphene for accelerating polysulfide redox and regulating Li plating. *Angewandte Chemie* 2022;134. DOI
64. Hou H, Shao L, Zhang Y, Zou G, Chen J, Ji X. Large-area carbon nanosheets doped with phosphorus: a high-performance anode material for sodium-ion batteries. *Adv Sci* 2017;4:1600243. DOI PubMed PMC
65. Liu T, Zhang Y, Hou J, Lu S, Jiang J, Xu M. High performance mesoporous C@Se composite cathodes derived from Ni-based MOFs for Li-Se atteries. *RSC Adv* 2015;5:84038-43. DOI
66. Ma C, Wang H, Zhao X, et al. Porous bamboo-derived carbon as selenium host for advanced lithium/sodium-selenium batteries. *Energy Technol* 2020;8:1901445. DOI
67. Fang R, Xia Y, Liang C, et al. Supercritical CO₂-assisted synthesis of 3D porous SiOC/Se cathode for ultrahigh areal capacity and long cycle life Li-Se batteries. *J Mater Chem A* 2018;6:24773-82. DOI
68. Wang C, Dong W, Wang L, et al. Dual catalysis-adsorption function modified separator towards high-performance Li-Se battery. *Appl Surf Sci* 2022;599:153932. DOI
69. Mo Y, Guo L, Jin H, et al. Improved cycling stability of LiNi_{0.6}Co_{0.2}Mn_{0.2}O₂ through microstructure consolidation by TiO₂ coating for Li-ion batteries. *J. Power Sources* 2020;448:227439. DOI
70. Jiang Z, Zeng Z, Hu W, Han Z, Cheng S, Xie J. Diluted high concentration electrolyte with dual effects for practical lithium-sulfur batteries. *Energy Storage Materials* 2021;36:333-40. DOI
71. Wang X, Tan Y, Liu Z, et al. New insight into the confinement effect of microporous carbon in Li/Se battery chemistry: a cathode with enhanced conductivity. *Small* 2020;16:e2000266. DOI
72. Wang B, Zhang J, Xia Z, et al. Polyaniline-coated selenium/carbon composites encapsulated in graphene as efficient cathodes for Li-

- Se batteries. *Nano Res* 2018;11:2460-9. DOI
73. Ryu HS, Guo Z, Ahn HJ, Cho GB, Liu H. Investigation of discharge reaction mechanism of lithium|liquid electrolyte|sulfur battery. *J Power Sources* 2009;189:1179-83. DOI
74. Yangdan L, Yichuan G, Yang T, Haichao T, Zhizhen Y, Jianguo L. Porous carbon derived from corncob as cathode host for Li-Se battery. *Ionics* 2022;28:2593-601. DOI
75. Ou J, Wang H, Wang J, Wu S. Porous carbon/Se composite derived from pistachio shell as high-performance Li-Se battery cathode. *Chem Lett* 2021;50:1797-800. DOI
76. Cao Y, Lei F, Li Y, et al. A MOF-derived carbon host associated with Fe and Co single atoms for Li-Se batteries. *J Mater Chem A* 2021;9:16196-207. DOI
77. Li HY, Li F, Wang YY, et al. Selenium confined in ZIF-8 derived porous carbon@MWCNTs 3D networks: tailoring reaction kinetics for high performance lithium-selenium batteries. *Chem Synth* 2022;2:8. DOI
78. Beer C, Barendse PS, Pillay P, Bullecks B, Rengaswamy R. Classification of high-temperature PEM fuel cell degradation mechanisms using equivalent circuits. *IEEE Trans Ind Electron* 2015;62:5265-74. DOI
79. Majasan JO, Cho JIS, Maier M, Dedigama I, Shearing PR, Brett DJ. Effect of anode flow channel depth on the performance of polymer electrolyte membrane water electrolyser. *ECS Trans* 2018;85:1593-603. DOI
80. Wu Q, Wang Y, Li P, Chen S, Wu F. MXene titanium carbide synthesized by hexagonal titanium aluminum carbide with high specific capacitance and low impedance. *Dalton Trans* 2022;51:3263-74. DOI
81. Yin J, Chen P, Lu M, et al. Cu-doped CoS₂ polyhedrons with high catalytic activity and long-term stability. *Sci China Mater* 2020;63:1337-44. DOI
82. Wang B, Li Z, Zhang J, et al. N-Doped 3D Interconnected carbon bubbles as anode materials for lithium-ion and sodium-ion storage with excellent performance. *J Nanosci Nanotechnol* 2019;19:7301-7. DOI
83. Hu Y, Fan L, Rao AM, et al. Cyclic-anion salt for high-voltage stable potassium-metal batteries. *Natl Sci Rev* 2022;9:nwac134. DOI PubMed PMC
84. Liu S, Li Y, Zhang Y, et al. In situ generation of AlF₃ in nanoporous carbon to enable cathode-electrolyte interface construction for stable Li-Se batteries. *ACS Appl Nano Mater* 2023;6:5414-21. DOI
85. Zhou M, Dong W, Xu A, et al. Surface iodine modification inducing robust CEI enables ultra-stable Li-Se batteries. *Chem Eng J* 2023;455:140803. DOI